

Measurements relating fire radiative energy density and surface fuel consumption – RxCADRE 2011 and 2012

Andrew T. Hudak^{A,F}, Matthew B. Dickinson^B, Benjamin C. Bright^A,
Robert L. Kremens^C, E. Louise Loudermilk^D, Joseph J. O'Brien^D,
Benjamin S. Hornsby^D and Roger D. Ottmar^E

^AUSDA Forest Service Rocky Mountain Research Station, Forestry Sciences Laboratory,
1221 South Main Street, Moscow, ID 83843, USA.

^BUSDA Forest Service, Northern Research Station, 359 Main Road, Delaware, OH 43015, USA.

^CRochester Institute of Technology, Center for Imaging Science, 54 Lomb Memorial Drive,
Rochester, NY 14623, USA.

^DUSDA Forest Service, Southern Research Station, Center for Forest Disturbance Science,
320 Green Street, Athens, GA 30602, USA.

^EUSDA Forest Service, Pacific Northwest Research Station, Pacific Wildland Fire Sciences
Laboratory, 400 North 34th Street, Suite 201, Seattle, WA 98103, USA.

^FCorresponding author. Email: ahudak@fs.fed.us

Abstract. Small-scale experiments have demonstrated that fire radiative energy is linearly related to fuel combusted but such a relationship has not been shown at the landscape level of prescribed fires. This paper presents field and remotely sensed measures of pre-fire fuel loads, consumption, fire radiative energy density (FRED) and fire radiative power flux density (FRFD), from which FRED is integrated, across forested and non-forested RxCADRE 2011 and 2012 burn blocks. Airborne longwave infrared (LWIR) image time series were calibrated to FRFD and integrated to provide FRED. Surface fuel loads measured in clip sample plots were predicted across burn blocks from airborne lidar-derived metrics. Maps of surface fuels and FRED were corrected for occlusion of the radiometric signal by the overstorey canopy in the forested blocks, and FRED maps were further corrected for temporal and spatial undersampling of FRFD. Fuel consumption predicted from FRED derived from both airborne LWIR imagery and various ground validation sensors approached a linear relationship with observed fuel consumption, which matched our expectation. These field, airborne lidar and LWIR image datasets, both before and after calibrations and corrections have been applied, will be made publicly available from a permanent archive for further analysis and to facilitate fire modelling.

Additional keywords: fire radiative energy (FRE), fire radiative power (FRP), fuel map, LiDAR, long-wave infrared (LWIR), RxCADRE.

Received 11 September 2014, accepted 11 May 2015, published online 28 July 2015

Introduction

The physical process of vegetation biomass burning greatly influences terrestrial ecosystem structure and function, at spatial scales ranging from biomes where fires affect the Earth system (forest, savanna and grassland) (Seiler and Crutzen 1980; Bowman *et al.* 2009) to the landscape level where humans apply prescribed fires and other vegetation management decisions (Lavorel *et al.* 2007; Trigg and Roy 2007). Prior remote sensing investigations to measure biomass burning rates also range broadly in scale, from coarse spatial resolution global monitoring satellites (Roberts and Wooster 2008) to airborne thermal imaging platforms (Riggan *et al.* 2004) with high resolution more suited to monitoring individual wildfires.

Geostationary satellites such as Meteosat carry a spinning enhanced visible and infrared imager (SEVIRI) sensor (Wooster *et al.* 2005; Roberts and Wooster 2008; Wooster *et al.* 2013), which has coarse spatial resolution (3 km) but is well suited for regional–global scale studies of combusted biomass estimated from fire radiative energy (FRE) measured in joules (J), which are integrated over time from repeated measures of fire radiative power (FRP) measured in watts (J s^{-1}). The polar-orbiting Terra and Aqua satellites bear the Moderate Resolution Imaging Spectroradiometer (MODIS) sensor, which has higher spatial resolution (1 km) yet provides FRP measures only twice daily at best (Roberts *et al.* 2011), thus necessitating fusion with burn area maps or other approaches to estimate FRE (Boschetti and

Roy 2009; Freeborn *et al.* 2010; Kumar *et al.* 2011). Dickinson *et al.* (2015) provide more details on active fire detection and FRP estimation from MODIS as well as Visible Infrared Imaging Radiometer Suite (VIIRS) imagery from which both 750-m and 375-m resolution active fire products are derived (Schroeder *et al.* 2014).

Wooster *et al.* (2005) demonstrated in small-scale (<2 m²) burning experiments using a variety of herbaceous and woody fuels that FRP is linearly related to biomass combustion rate, and that FRE is linearly related to biomass combusted (see also Freeborn *et al.* 2010 and Kremens *et al.* 2012). The latter quantity represents a greater measurement challenge because it requires sufficient sampling over time to integrate FRE from instantaneous measures of FRP. Temporal sampling resolution of active fire by fixed-wing aircraft is limited to 2–3 min, the rate at which the same airspace can be revisited. Riggan *et al.* (2004) used airborne active fire imagery to estimate carbon and energy fluxes from individual fires in Brazil. However, integration of total FRE from airborne FRP image time series collected over the entire duration and spatial extent of a landscape-level fire has not yet been achieved.

The prediction of surface fuel loads, including those beneath a forest canopy, using the canopy-penetrating and three-dimensional capability of airborne lidar is yet to be achieved. Seielstad and Queen (2003) described the potential of airborne lidar for differentiating between surface fuel models in lodgepole pine (*Pinus contorta* Douglas ex Loudon) forests. Terrestrial lidar has been used to classify surface fuel types within high-resolution fuel cells in fire-maintained longleaf pine forests (Hiers *et al.* 2009; Loudermilk *et al.* 2009, 2012), and Rowell and Seielstad (2015) showed that terrestrial lidar can be used in concert with an airborne lidar-derived digital terrain model (DTM) to characterise surface fuel heights at high resolution. However, surface fuel loads like those beneath the longleaf pine forests occurring at Eglin Air Force Base (AFB) in Florida, the site of these RxCADRE prescribed fires, have not been predicted as a continuous variable from airborne lidar.

The primary objective in this paper was to predict fuel consumption from estimates of FRE at multiple scales ranging from plots (<1 ha) to large burn blocks (>100 ha). The related secondary objective was to predict surface fuel loads and fuel combusted across these same areas. Our chosen blocks were burned with prescribed fires at Eglin AFB in 2011 and 2012 as part of the RxCADRE project and imaged by both the Wildfire Airborne Sensor Platform (WASP) longwave infrared LWIR sensor and a scanning lidar sensor mounted aboard the same aircraft.

Methods

Prescribed burn blocks

This paper considers the prescribed RxCADRE fires conducted in selected land blocks at Eglin AFB in 2011 and 2012. The two 2011 burns of forested blocks '703C' and '608A' were ignited by aerially delivered, delayed-ignition devices dispensed from a helicopter in strips at right angles to and successively into the ambient wind direction. The nine blocks burned on the 'B70' range in 2012 were lit with drip torches on the upwind side to produce a more natural fireline progression through the blocks.

Like the two 2011 blocks, one large block (L2F) was forest dominated by longleaf pine (*Pinus palustris* Mill.), whereas the other two large (L1G and L2G) and six small blocks (S3, S4, S5, S7, S8 and S9) were non-forested. Surface fuels were composed of variable proportions of grasses, forbs and shrubs dominated by turkey oak (*Quercus cerris* L.). Further details regarding the prescribed fires may be found in Ottmar *et al.* (2015b).

Ground measures

Surface fuel loads were measured by destructive harvesting in 1 × 1-m clip plots within all burn blocks except L2F, where clip plots were 0.5 × 0.5-m. The pre- and post-fire clip plot positions alternated across a given sample unit, so consumption could not be estimated at the plot level (i.e. consumption estimates were limited in resolution to the sample unit level). A sample unit consisted of a set of clip plots arranged systematically in one of three configurations: (1) surrounding a 40 × 40-m (2011) or 20 × 20-m (2012) highly instrumented plot (HIP) that was randomly located within a representative fuel condition inside a large burn block (with two to three HIPs per large burn block); (2) surrounding a 200 × 100-m small burn block; or (3) along parallel transects from a random starting point within a large burn block. Details on the fuel sampling protocols can be found in Ottmar *et al.* (2015a).

As litter decomposes, the various herbaceous and woody components become indistinguishable to form (beneath the litter) a highly degraded layer of material known as duff that eventually will be incorporated into the soil – unless consumed by fire. Ottmar *et al.* (2015a) did not include duff measures in their analysis because measurable duff depths were only encountered in the L2F burn block. We include the L2F duff measures in this analysis because burning duff also contributes to radiative energy flux. Duff depths were measured at the L2F sample plots where duff occurred; elsewhere zeroes were recorded.

Various ground sensors were deployed to collect voltage data calibrated to fire radiative power flux density (FRFD, W m⁻²) time series that were subsequently integrated over time to provide independent measures of fire radiative energy density (FRED, J m⁻²) for this analysis. Radiometers and infrared (IR) cameras were usually deployed inside a HIP. O'Brien *et al.* (2015) provide sensor specifications for IR cameras, which were either nadir viewing and deployed on a 8.2-m tripod within the large burn block HIPs in 2011 and 2012 and the small burn blocks in 2012; or oblique viewing and deployed on a 26-m boom lift parked outside the fire perimeter for a synoptic view of the six small burn blocks (O'Brien *et al.* 2015). Dickinson *et al.* (2015) provide sensor specifications on nadir-viewing, dual-band 'pocket' radiometers deployed on a 0.5-m arm and elevated to 5.5 m on telescoping poles, with a field of view of 52.5° for full power and 75° for partial power. Dual-band 'pocket' radiometers deployed by Dickinson *et al.* differed from 'orange box' radiometers used by O'Brien *et al.* in their field of view and bandpass. Upon calibration, both types of radiometers measure FRFD and allow estimates of FRED.

Airborne lidar

Airborne discrete-return lidar data were collected by Kucera International using a Leica ALS60 sensor on 5 February 2011

(703C burn block), 6 February 2011 (608A burn block) and 3 November 2012 (B70 burn blocks). Vertical uncertainty quantified with root mean squared error (RMSE), comparing the laser-measured ground heights to independent ground control points (GCPs) geolocated with a resource-grade global positioning system (GPS, Trimble Pathfinder ProXT), was 0.600 m at burn block 703C ($n = 9$ GCPs) and 0.642 m at burn block 608A ($n = 12$ GCPs) in 2011. In 2012, installation of survey-grade GCPs ($n = 20$) reduced the vertical uncertainty by almost an order of magnitude (RMSE = 0.082 m). However, average vertical bias was comparable between all three lidar collections (−0.010 m at 703C, 0.003 m at 608A, 0.007 m at B70), as were the flight and lidar sensor operation parameters (Table 1). Terascan software was used to classify and edit the lidar data.

A 1-m DTM was interpolated from the vendor-classified ground returns using the GridSurfaceCreate function of FUSION software (McGaughey 2014). The ‘minimum’ value was used rather than the default ‘mean’, such that the DTM took the value of the minimum elevation value in each grid cell. This lowers the DTM slightly so that the majority of near-ground returns will be above the DTM and hence have positive height values.

The ClipData function of FUSION was used to clip ~200–300 points within a 3-m radius of clip plot centre coordinates. The DTM was subtracted from the point cloud to normalise absolute point heights to relative heights above ground. Using the CloudMetrics function of FUSION, canopy height and density metrics were calculated from lidar returns 0–2 m above ground and within a 3-m radius of each pre-fire clip plot. Candidate metrics for predictive modelling included the mean, mode, standard deviation (s.d.), coefficient of variation (c.v.), skewness and kurtosis statistics calculated across the 0–2 m

height range; as well as mean, mode, s.d., c.v. and proportion of all returns calculated within vertical strata of 0–0.05, 0.05–0.15, 0.15–0.50 and 0.50–1.0 m above ground. The stratum depths were intended to be unequal because the lidar returns are denser nearer the ground, where there is more vegetation and fuel to intercept the laser pulses, than higher above the ground.

The plot-level lidar metrics were considered as candidate predictor variables in a multiple linear regression model, using the ‘lm’ function in R (R Core Team 2014). The Shapiro–Wilk W statistic was used to test the response variable for normality, and Moran’s I statistic was used to test model residuals for spatial autocorrelation. Predictions were tested for dissimilarity with observations using a bootstrap test for equivalence (Robinson *et al.* 2005). Best subsets regression (using the ‘regsubsets’ function in the ‘leaps’ package of R) was employed to select the best predictors from the candidate metrics; minimising the Akaike Information Criterion (AIC) statistic was the criterion used to choose the best subset model, following the approach of Hudak *et al.* (2006). The FUSION GridMetrics function was used to create gridded rasters of selected metrics at 5-m resolution for mapping. Overstorey canopy cover was calculated as the percentage of first returns above breast height (1.37 m) (Hall *et al.* 2005; Kim *et al.* 2009).

Airborne LWIR imagery

The airborne WASP LWIR sensor (McKeown *et al.* 2004) imaged the active fires within the five large burn blocks. WASP has a nominal 8–9.2- μm bandwidth (for further details see Dickinson *et al.* 2015). Image frames were collected at 3- or 4-s intervals (Table 2). Using the ArcPy package in Python, raw WASP LWIR digital numbers were calibrated first to sensor-reaching radiance, L_{LWIR} ($\text{W m}^{-2} \text{sr}^{-1}$) for the passband of the WASP LWIR detector (Eqn 1). The spectral response of the WASP LWIR detector that defines the passband is known from laboratory measurements and was used in the calculation of L_{LWIR} . Ground-leaving excitation, or observed FRFD ($FRFD_{obs}$) (W m^{-2}) (Eqn 2), is then calculated in two steps as follows:

$$L_{LWIR} = f(DN) = 2 \times 10^{-6} DN^2 + 0.0176 DN \quad (1)$$

$$FRFD_{obs} = \pi b (L_{LWIR})^M \quad (2)$$

where DN is digital number, and b and M vary by WASP LWIR acquisition (Table 2) because of variable atmospheric

Table 1. Parameters of airborne lidar collected immediately before the 2011 and 2012 RxCADRE prescribed burns

Lidar collection parameter	2011	2012
Flying height above ground level	1200 m	1200 m
Sidelap	50%	50%
Field of view	24°	20°
Pulse rate	176.1 kHz	178.6 kHz
Average point density	6.9 points m^{-2}	6.8 points m^{-2}

Table 2. Burn block names, burn dates, WASP LWIR calibration coefficients (power fit; Eqn 2) and sampling characteristics of the 2011 and 2012 RxCADRE prescribed burns at Eglin AFB

Temporal undersampling proportion is the proportion of time during which WASP was not imaging the burn block. Spatial undersampling proportion is the average proportion of the burn block not imaged in individual WASP frames

Burn block	Burn date	b	M	WASP LWIR spatial resolution (m)	WASP LWIR sampling interval (s)	Temporally undersampled proportion	Spatially undersampled proportion
703C	6 February 2011	5.216	1.374	2.8	4	0.69	0.70
608A	8 February 2011	5.138	1.374	2	4	0.68	0.85
L1G	4 November 2012	7.282	1.393	3	3	0.76	0.63
L2G	10 November 2012	7.006	1.380	3	3	0.85	0.35
L2F	11 November 2012	6.718	1.385	1.5	3	0.85	0.68

absorption that was simulated with the Moderate Resolution Atmospheric Transmission algorithm (MODTRAN) (Berk *et al.* 2003) based on atmospheric profiles of temperature and humidity during the burning period. Equation 1 was parameterised using a blackbody in the laboratory. MODTRAN runs and further details regarding WASP LWIR image calibration are described in Accessory Publication 1 associated with Dickinson *et al.* (2015).

For each burn block, calibrated image frames were assembled into a multi-layer stack with a common origin, grain and extent. This realigns the pixels at a common resolution based on the nominal resolution of the image frames (Table 2). Small shifts in the pixel coordinates necessitate reassignment of the pixel values to the shifted locations; nearest neighbour resampling was used because it preserves the pixel values from the input image frames, making it minimally disruptive.

FRED (J m^{-2}) was calculated from image time series of calibrated FRFD (W m^{-2}). Fire pixels were separated from non-fire pixels using a threshold of 1070 W m^{-2} derived independently from the pocket radiometer data. The threshold can be thought of as the post-fire FRFD value asymptotically approached by a pixel as it cools after burnover, making it greater than the apparent FRFD of unburned (background) pixels masked from consideration. To estimate the threshold, the peak FRFD was determined from the pocket radiometer datasets ($n = 60$) distributed at fixed locations across all of the 2012 prescribed burns and sampling over the duration of the fires at 5-s intervals. For each dataset, FRFD measurements from before the peak were removed and the time rescaled so that peak time was assigned a value of $t = 0$. Then, parameters of a negative exponential model with an offset (the threshold) were fit to the individual datasets and the average threshold and its confidence interval determined from the results. The threshold was determined to be 1070 W m^{-2} , with no significant difference between radiometers in the forested *vs.* non-forested blocks. Observed FRED ($FRED_{obs}$) at each fire pixel, defined as having a minimum of one FRFD observation $> 1070 \text{ W m}^{-2}$, was calculated following the trapezoidal rule for numerical integration that was employed for the same purpose by Boschetti and Roy (2009), by Eqn 3:

$$FRED_{obs} = \sum_i^n 0.5(FRFD_i + FRFD_{i-1})(t_i - t_{i-1}) \quad (3)$$

where $FRFD_i$ is pixel-level FRFD from each image i in the time series, and t is time in seconds. If pixel vectors only contained one FRFD measurement, then FRED was calculated by multiplying the single FRFD measurement by the sampling interval of either 3 s (2012) or 4 s (2011), depending on the burn block (Table 2). Most pixel vectors contained only one FRFD measurement for FRED calculation; 86, 92, 95, 96 and 88% of FRFD pixel vectors for 608A, 703C, L1G, L2G, and L2F, respectively.

Corrections for sampling biases

Back-transformation of the surface fuel model predictions from the natural log (ln) scale to the natural scale introduced bias. Therefore, a bias correction factor (c_b) was calculated based on

the mean square error (MSE) of the model residuals following Baskerville (1972), by Eqn 4:

$$c_b = \exp^{(0.5MSE)} \quad (4)$$

where predicted fuels upon back-transformation were multiplied by c_b .

A source of bias in both observed and predicted fuel loads was the exclusion of duff at the L2F block. Duff load was not measured at any RxCADRE burns except L2F and was therefore excluded from the fuel loads reported by Ottmar *et al.* (2015a). However, duff load was measured at L2F because substantial duff was evident in the field given that it had not burned for 3 years, longer than the other 2012 or 2011 burn blocks. Therefore, the pre-fire fuel load was increased by the percentage consumption observed in L2F across the other fuel types. Duff consumption was similarly increased under the assumption that the same proportion of duff was consumed as was observed across the other fuel types. Percentage consumption of duff most likely did differ from the other fuel types; for example, due to higher duff fuel moisture (which we did not measure). However, given that there was measurable charred duff, which undoubtedly contributed to the FRE flux, we judged it more accurate to estimate duff consumption under this simple assumption than to ignore it. The duff corrections were applied to both observations (field based) and predictions (lidar based) of surface fuel load and consumption.

Both the lidar-derived surface fuel maps and the WASP LWIR-derived FRED maps were affected by occlusion of the radiometric signal by the overstorey canopy in the forested blocks. Canopy interception was assumed to equally affect the airborne lidar and LWIR radiation signals. Canopy cover grids were generated with the same origin, grain and extent as the lidar-derived surface fuel maps or the WASP LWIR-derived FRED maps requiring correction. Maps of predicted surface fuel ($Fuel_{pre}$) were multiplied with corresponding maps of canopy cover proportion (c_c) generated within matching pixels, by Eqn 5:

$$Fuel_{cc} = Fuel_{pre}(1 + c_c) \quad (5)$$

to produce maps of canopy-corrected surface fuel, $Fuel_{cc}$. Likewise, $FRED_{obs}$ (from Eqn 3) maps were multiplied with corresponding maps of canopy cover proportion (c_c) generated within matching pixels, by Eqn 6:

$$FRED_{cc} = FRED_{obs}(1 + c_c) \quad (6)$$

to produce maps of canopy-corrected FRED, $FRED_{cc}$.

The cumulative time that WASP LWIR was imaging the fire during passes was much less than the time required for the aircraft to return to the airspace above the fire between passes. This temporal undersampling of FRFD caused FRED to be underestimated. Therefore, the proportion of time that WASP LWIR was not actively imaging the burn block was calculated, as a correction for temporal undersampling bias.

The spatial extent (and resolution) of the WASP LWIR image frames depended on the flying height of the aircraft.

Usually, only part of a large burn block was imaged within each WASP LWIR frame. Such spatial undersampling missed fire activity outside the image frame, especially in the larger burn blocks such as 608A. This resulted in FRFD and FRED being underestimated upon aggregation to the extent of the entire burn block. Therefore, the proportion of the burn block not imaged in each WASP LWIR frame was calculated and averaged across all frames as a correction for spatial undersampling bias.

The correction factors for temporal and spatial undersampling biases by WASP LWIR were assumed to be additive, as applied in Eqn 7 to calculate a corrected FRED ($FRED_{cor}$):

$$FRED_{cor} = FRED(1 + c_t + c_s) \quad (7)$$

where $FRED$ is observed FRED ($FRED_{obs}$, by Eqn 3) averaged across the burn block, either with canopy cover correction ($FRED_{cc}$, by Eqn 6) in the forest blocks or without in the non-forest blocks; c_t is temporal undersampling proportion and c_s is spatial undersampling proportion.

Predicting fuel consumption from FRED

Predicting fuel consumption from FRED estimates derived from the ground-based IR cameras and dual-band radiometers required estimates of fire radiated fraction and an assumption of fuelbed heat of consumption. Kremens *et al.* (2012) estimated fire radiated fraction from 8 × 8-m experimental burn plots in mixed-oak fuelbeds; the experimental plot fuels included additions of milled woody fuels and resulted in a large range in fuel consumption (0.2–3.2 kg m⁻²). Predicted fuel consumption (FC_{pre}) was calculated following Reid and Robertson (2012) by Eqn 8 as follows:

$$FC_{pre} = FRED/rf/hc \quad (8)$$

where $FRED$ is either FRED derived from the various IR validation sensors deployed on the ground or $FRED_{cor}$ derived from WASP LWIR after applying corrections (Eqns 6,7); rf is fire radiated fraction (0.13–0.22) as estimated by Kremens *et al.* (2012) in mixed-oak fuelbeds; and hc is heat of combustion, which is assigned a constant value of 17.552 MJ kg⁻¹ and includes ash, as reported by Reid and Robertson (2012), working in natural longleaf pine savanna and old field fuelbeds, where the heat of combustion is of similar magnitude.

Results

Surface fuel load

A pre-fire duff load of 1.94 Mg ha⁻¹ at L2F was estimated by dividing the measured post-fire duff load of 1.14 Mg ha⁻¹ by the observed proportion of surface fuel consumed at L2F (0.5887) (Table 3). Adding estimated duff load and consumption in L2F translated to a 21.9% increase above the pre-fire surface fuel load and a 26.3% increase above the consumption reported by Ottmar *et al.* (2015a) (Table 3).

The response variable, pre-fire surface fuel load, was found to be significantly non-normal by the Shapiro–Wilk test for normality ($W = 0.721$, $P < 0.0001$), so a natural logarithm transform was applied ($W = 0.9554$, $P = 0.27$ after transformation). Nine lidar metrics were selected as the best subset of significant predictors in a multiple linear regression model (Table 4). Highly collinear predictors were avoided; thus, the highest Pearson correlation between the nine selected lidar metrics was 0.6. The model explained 44% of variance in ln-transformed surface fuel load and was highly significant (Fig. 1a). Spatial autocorrelation in the model residuals was found by the Moran's test to be weak and not significant ($I = 1.48$, $P = 0.07$). The pattern of model residuals plotted against the fitted values was random with no trend. The MSE

Table 3. Burn block names, areas and number of pre-fire clip plots (total = 354) used to predict surface fuels from airborne lidar metrics
Estimates of surface fuel load and consumption include estimates of duff load and consumption in the L2F burn block. The last column reports block-level means of the lidar-derived, overstorey canopy cover grids used to correct maps of surface fuels (Fig. 2) and FRED (Fig. 4) in the forested blocks

Burn block	Area (ha)	Clip plots included in fuel model (n)	Observed surface fuel load (Mg ha ^{-1A})	Observed absolute consumption (Mg ha ⁻¹)	Observed relative consumption (%)	Mean canopy cover proportion
703C	668	60	5.35	3.03	56.58	0.250
608A	828	40	5.97	4.68	79.12	0.227
L1G	454	57	2.15	1.54	72.66	0
L2G	127	57	3.57	3.09	85.33	0
L2F	151	65	10.80 ^A	6.36 ^B	58.87 ^C	0.373
S3	2	0 ^D	3.08	2.56	83.15	0
S4	2	0 ^D	2.45	2.04	83.30	0
S5	2	0 ^D	2.82	2.19	77.58	0
S7	2	25	4.11	1.80	43.82	0
S8	2	25	3.64	2.80	77.02	0
S9	2	25	2.42	1.40	57.76	0

^AFuel load reported by Ottmar *et al.* (2015a) (8.86 Mg ha⁻¹) was increased 21.9% to include duff.

^BConsumption reported by Ottmar *et al.* (2015a) (5.03 Mg ha⁻¹) was increased 26.3% to include duff.

^CSame percentage consumption as reported by Ottmar *et al.* (2015a); consistency was assumed when increasing observed pre-fire fuel load and consumption to include duff.

^DThe S3, S4 and S5 blocks were burned on 1 November 2012, 2 days before the lidar survey; therefore, fuel measures at the 75 clip plots at these three blocks (see Fig. 2) were excluded from the predictive model, whereas the 75 clip plots at blocks S7, S8 and S9 (see Fig. 2) burned on 7 November 2012 were included.

Table 4. Multiple linear regression model predicting surface fuel loads (ln-transformed) from nine selected lidar metrics

Lidar predictor	Estimate	Std. Error	<i>t</i> -value	Pr (> <i>t</i>)	Significance
(Intercept)	2.141	0.315	6.789	4.96e-11	***
Mean (0–2 m)	–1.767	0.780	–2.266	0.024	*
Kurtosis (0–2 m)	0.003	0.001	2.261	0.024	*
Mode (0–0.05 m)	–4.772	2.327	–2.051	0.041	*
Proportion (0–0.05 m)	–1.779	0.242	–7.355	1.41e-12	***
Proportion (0.05–0.15 m)	–1.777	0.308	–5.763	1.84e-08	***
s.d. (0.05–0.15 m)	23.838	8.616	2.767	0.006	**
c.v. (0.15–0.50 m)	0.575	0.210	2.743	0.006	**
s.d. (0.5–1 m)	1.507	0.677	2.225	0.027	*
s.d. (1–2 m)	0.988	0.368	2.687	0.008	**

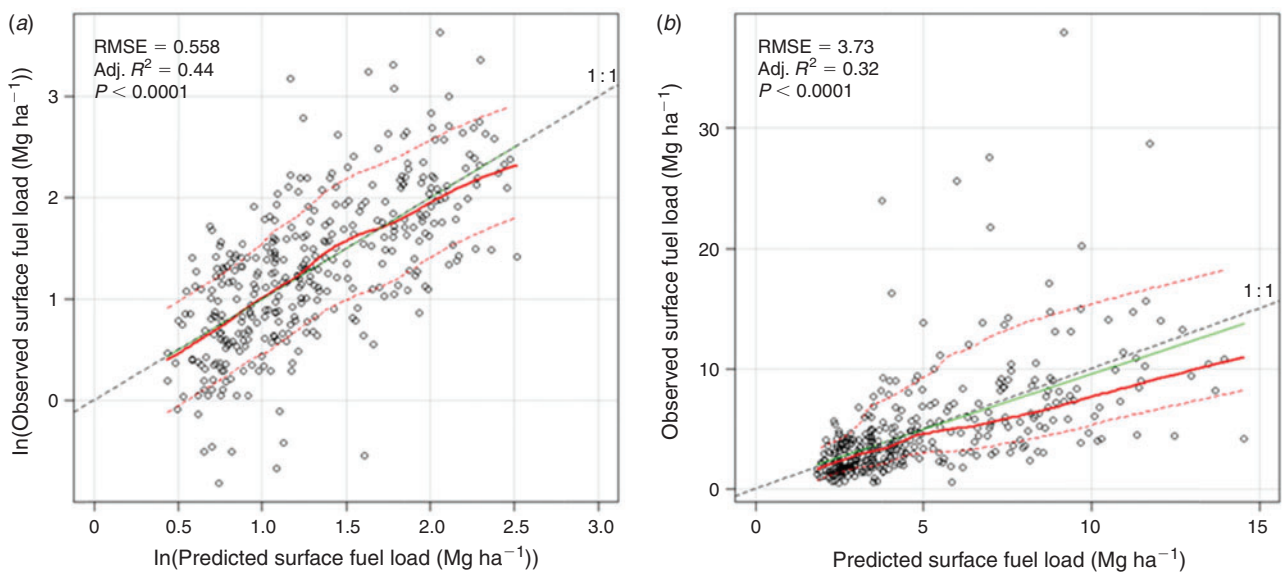


Fig. 1. Multiple linear regression models predicting *a*) pre-fire surface fuel load (ln-transformed) from nine airborne lidar metrics (Table 4). Back-transformation with bias correction yielded the predicted vs. observed relationships for surface fuel load in *b*). On both graphs, the line of best fit is shown in green, and the nonparametric regression with loess smoothing is shown in red, with the solid line indicating the mean fit and the dashed lines indicating the square root of the squared positive and negative residuals above and below the mean.

of the residuals was 0.32, which when substituted into Eqn 1, yielded a bias correction factor of 1.17 that was multiplied with the back-transformed predictions. Fig. 1*b* illustrates back-transformed, bias-corrected predictions vs. observations on the natural scale, with an RMSE of 3.73. Fig. 2 displays predicted surface fuel loads and fuel consumption (calculated from observed relative consumption, Table 3), with the higher fuel loadings and consumption in the forested blocks, particularly L2F, as was observed in the field. Surface fuel loads had accumulated for 3 years in L2F, for 2–3 years in L2G, for 2 years in 703C and 608A and for 1 year in L1G.

The range of fuel predictions was not as broad as the range of fuel observations made on the ground (Fig. 1). This is a consequence of the regression modelling approach, which tends to compress the distribution of predictions towards the mean. However, bootstrap tests of equivalence rejected the null

hypothesis of dissimilarity ($P = 0.025$), meaning that predictions were similar to observations and were neither biased nor disproportional (Robinson *et al.* 2005). Moreover, fuel load and consumption predictions when aggregated to the burn block level compared favourably with observations, especially after correcting for canopy cover occlusion in the three forested blocks (Figs 2, 3). Percentage canopy cover calculated from the airborne lidar returns above breast height (mean = 44%, s.d. = 20%) compared well with field measures of overstorey canopy closure (mean = 43%, s.d. = 22%) collected pre-fire at the L2F clip plots ($n = 60$) using a spherical densiometer held at breast height (Pearson correlation $r = 0.60$, $P < 0.0001$). As the gridded lidar measures of canopy cover (Table 3) were based on many orders of magnitude more data collected across the entire burn blocks, they were used to correct the surface fuel maps for canopy occlusion in a spatially explicit manner (Fig. 2).

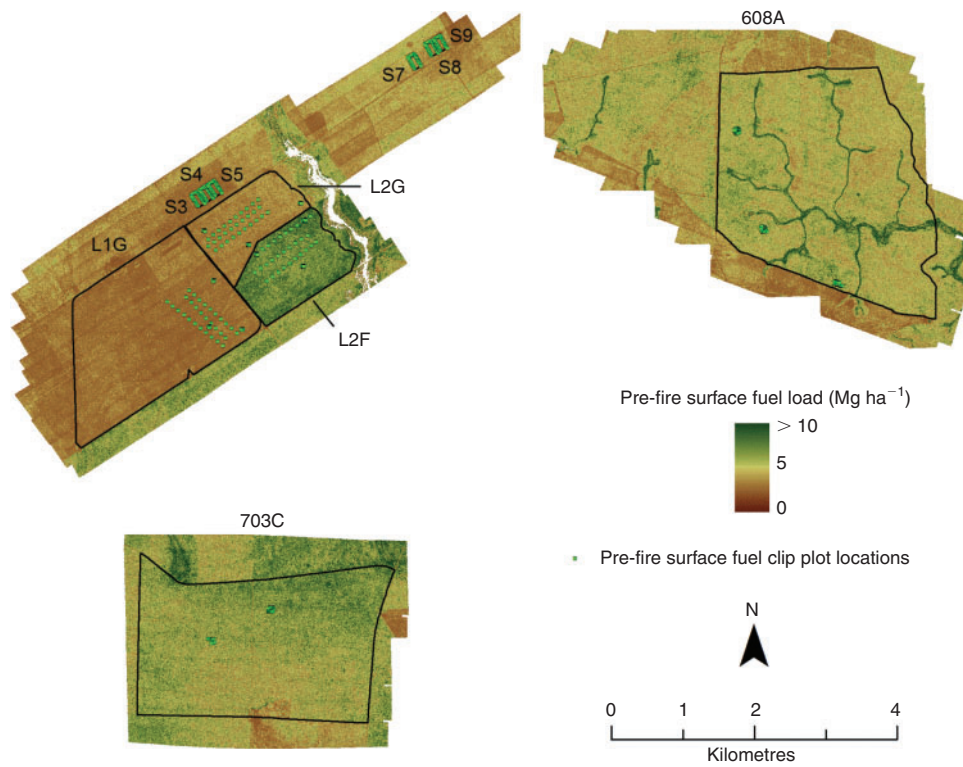


Fig. 2. Pre-fire surface fuels mapped across the extent of the 2011 and 2012 lidar collections based on the predictive models in Fig. 1 and lidar metrics in Table 4. See fig. 1 in Ottmar *et al.* (2015a, 2015b) for the locations of these burn blocks within Eglin AFB. Correction for overstorey canopy occlusion in the forested areas has been applied.

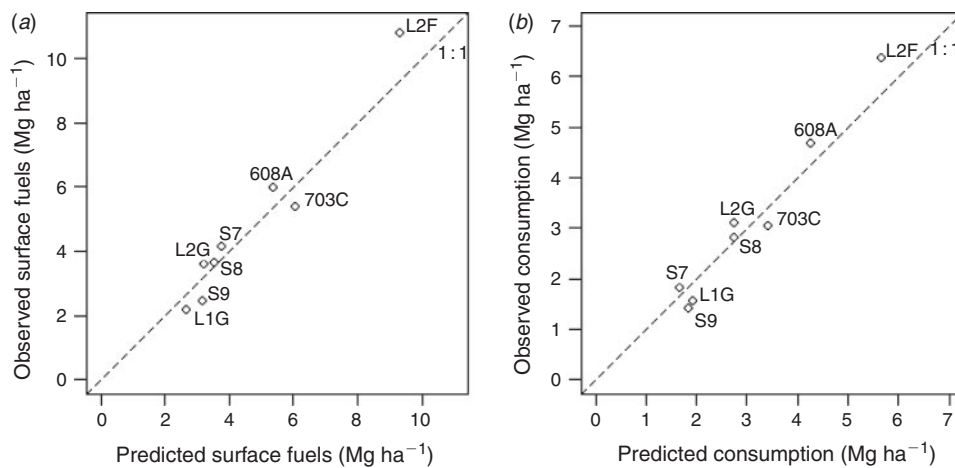


Fig. 3. Burn block-level comparisons between *a*) surface fuels predicted from selected pre-fire lidar metrics (Table 4) vs. pre-fire surface fuels observed (Table 3), and *b*) consumption predicted (by multiplying mean block-level surface fuels predicted in *a*) by proportion consumed, Table 3) vs. consumption observed. Correction for overstorey canopy occlusion in the forested blocks has been applied to predictions in both graphs. Both the observation and the prediction for the L2F block have been corrected for duff presence.

Fire radiative energy density

The FRED maps in the three forested blocks were corrected for overstorey occlusion with the same lidar-derived, canopy cover metric as the surface fuel maps. The broader spatial patterns

evident in the FRED maps of the 608A and L2F burn blocks (Fig. 4) relate reasonably well to the greater patchiness in fuel conditions in these blocks (Fig. 2). However, the more obvious pattern in the FRED images is the apparent parallel firelines,

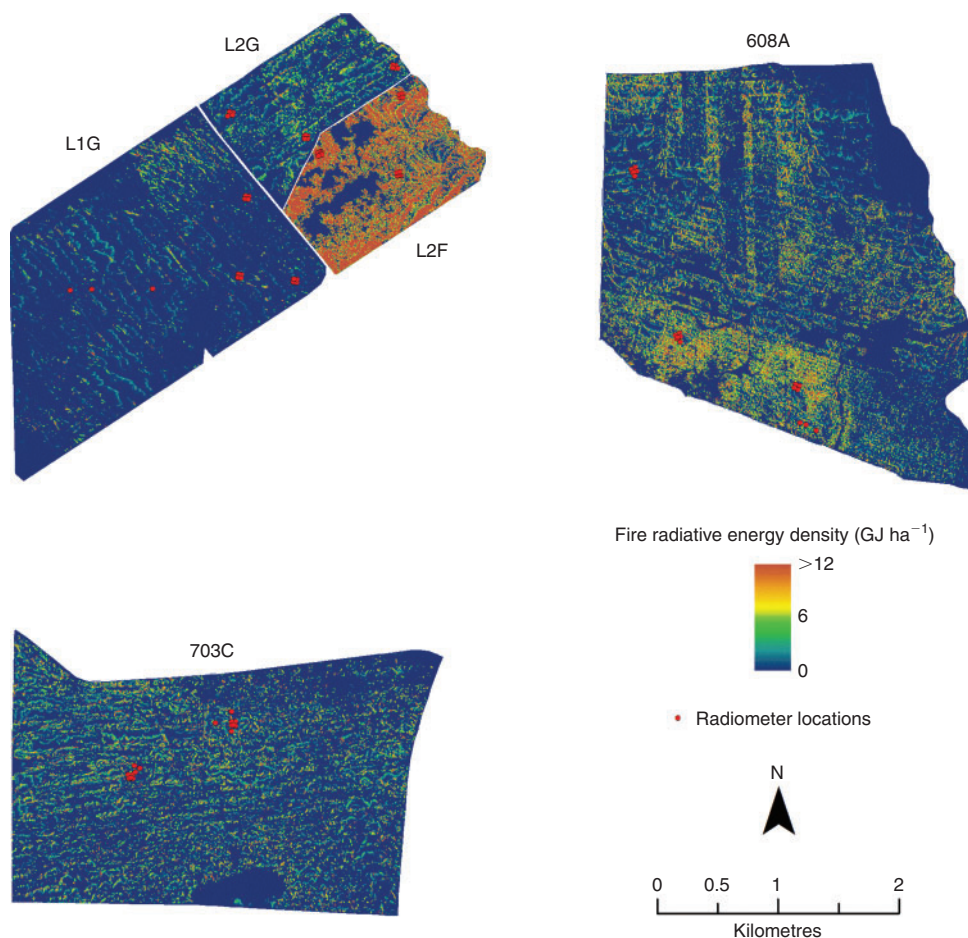


Fig. 4. FRED estimated from WASP LWIR-derived FRFD image time series collected across the extent of the 2011 and 2012 large burn blocks. See [fig. 1 in Ottmar *et al.* \(2015a, 2015b\)](#) for the locations of these burn blocks within Eglin AFB. Correction for overstorey canopy occlusion in the forested blocks has been applied.

which are an artefact of temporal undersampling ([Fig. 4](#)). The blue voids between the apparent firelines are typically not actual voids in surface fuel loads but ‘blind spots’ where the aircraft was outside the airspace above the burn block when flame fronts spread through them ([Fig. 4](#)). They are most apparent in the L1G block where fuel loads were lightest ([Ottmar *et al.* 2015a](#)) and the fire residence time and cooling period in a given pixel was least ([O’Brien *et al.* 2015](#)). The opposite extreme can be observed in the apparent lack of firelines throughout much of the L2F block, where surface fuel loads were heaviest and fire residence times and cooling periods were longest ([Fig. 4](#)). In the 703C and 608A blocks, patterns of FRFD (not shown) and FRED ([Fig. 4](#)) reflect numerous, simultaneous aerial ignitions from a helicopter.

The more localised effect of the moving fireline on FRFD sampling intervals is illustrated in [Fig. 5](#), comparing imagery between airborne WASP LWIR and nadir-viewing IR cameras deployed on the ground. The nadir IR cameras located within the HIPs imaged a restricted but fixed field of view continuously at 1- to 6-s intervals (depending on camera used). Thus, the data are not temporally undersampled like WASP LWIR. For instance, of the 10 HIPs with coincident nadir IR camera and WASP

LWIR measures of FRFD, WASP LWIR captured peak FRFD only twice (608A HIP SE, L1G HIP 2) ([Fig. 5](#)).

Spatial undersampling was a smaller source of bias than temporal undersampling in the 2012 burn blocks but was a larger source for the especially large 608A block burned in 2011 ([Table 2](#)). Because the aircraft pilot sought to maximise coverage of the fire with each pass, the centre of the burn blocks was more frequently imaged than some of the edges parallel to the flight path.

Relationship between fuel consumption and FRED

Thermal radiation sensors on the ground provided a means to validate the estimates of FRED generated from WASP LWIR, but without temporal and spatial undersampling. Predictions of fuel consumption based on observations of FRED and [Eqn 8](#) facilitated more direct comparison between ground-based sensor types and WASP LWIR, on whether predictions and observations deviated from a 1:1 relationship ([Fig. 6](#)). Compared with observed consumption, consumption calculated from FRED at midpoint radiated fraction ([Kremens *et al.* 2012](#)) was under-predicted from the orange box radiometers

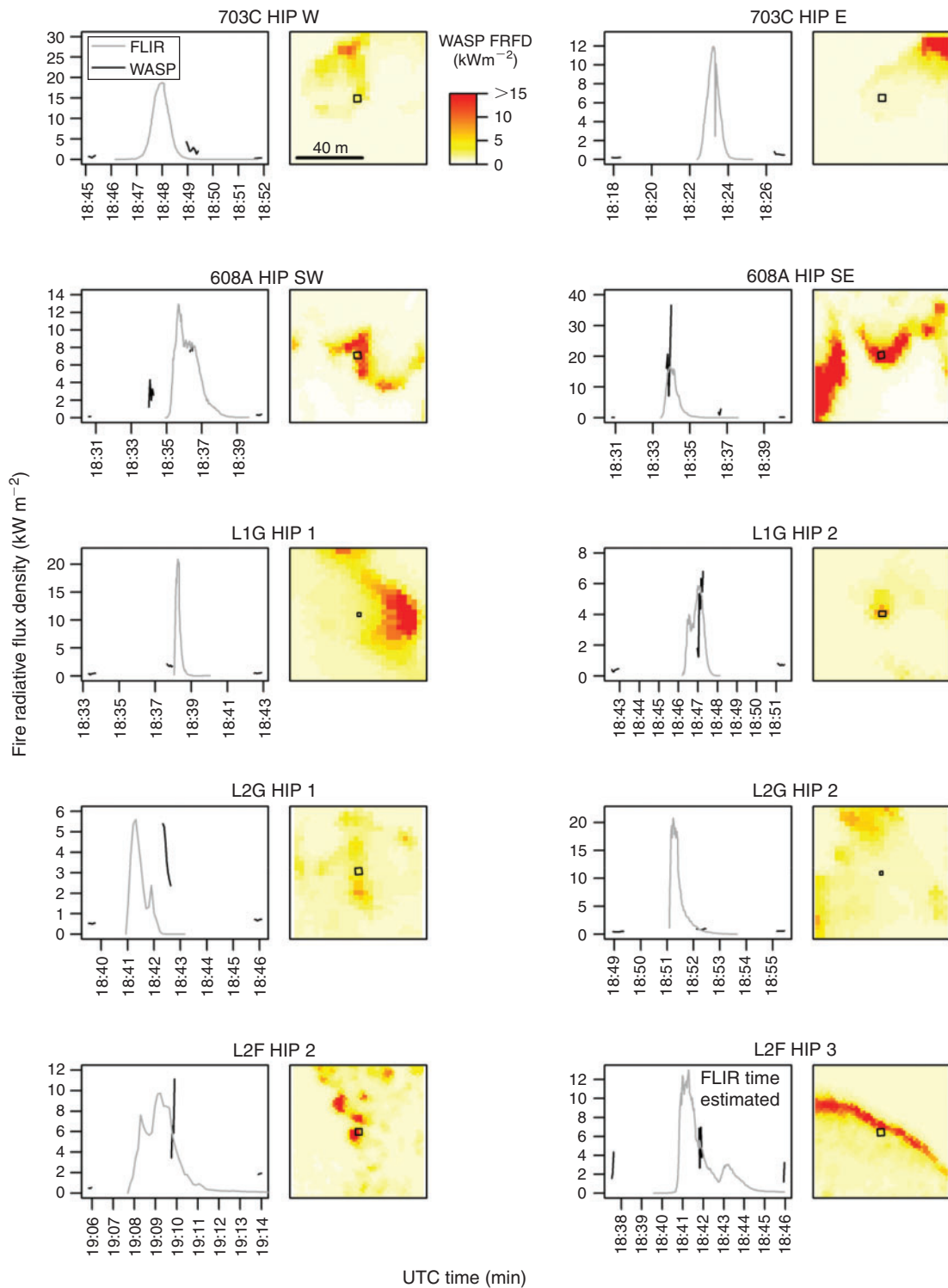


Fig. 5. FRFD estimated at the scale of 10 tripod-mounted, nadir-viewing IR cameras at the large burn block HIPs. The figure illustrates FRFD measured at two HIPs (columns) per each of the five large burn blocks (rows). Line graphs (on left of each pair) show the intermittent FRFD record obtained from WASP LWIR imagery compared with the FRFD recorded by the IR cameras as the flame front passed beneath. Heat images (on right of each pair) illustrate the closest position of the flame front to the IR camera field of view (tiny black box) as observed with WASP LWIR. The intention is to show temporal undersampling of WASP LWIR, which entirely missed the flame front in more cases than it captured peak FRFD at these fixed locations. (Note: Although the relative times recorded by the IR camera at L2F HIP 3 are accurate, the absolute times in the lower right graph are estimated because the start time failed to synchronise with UTC time.)

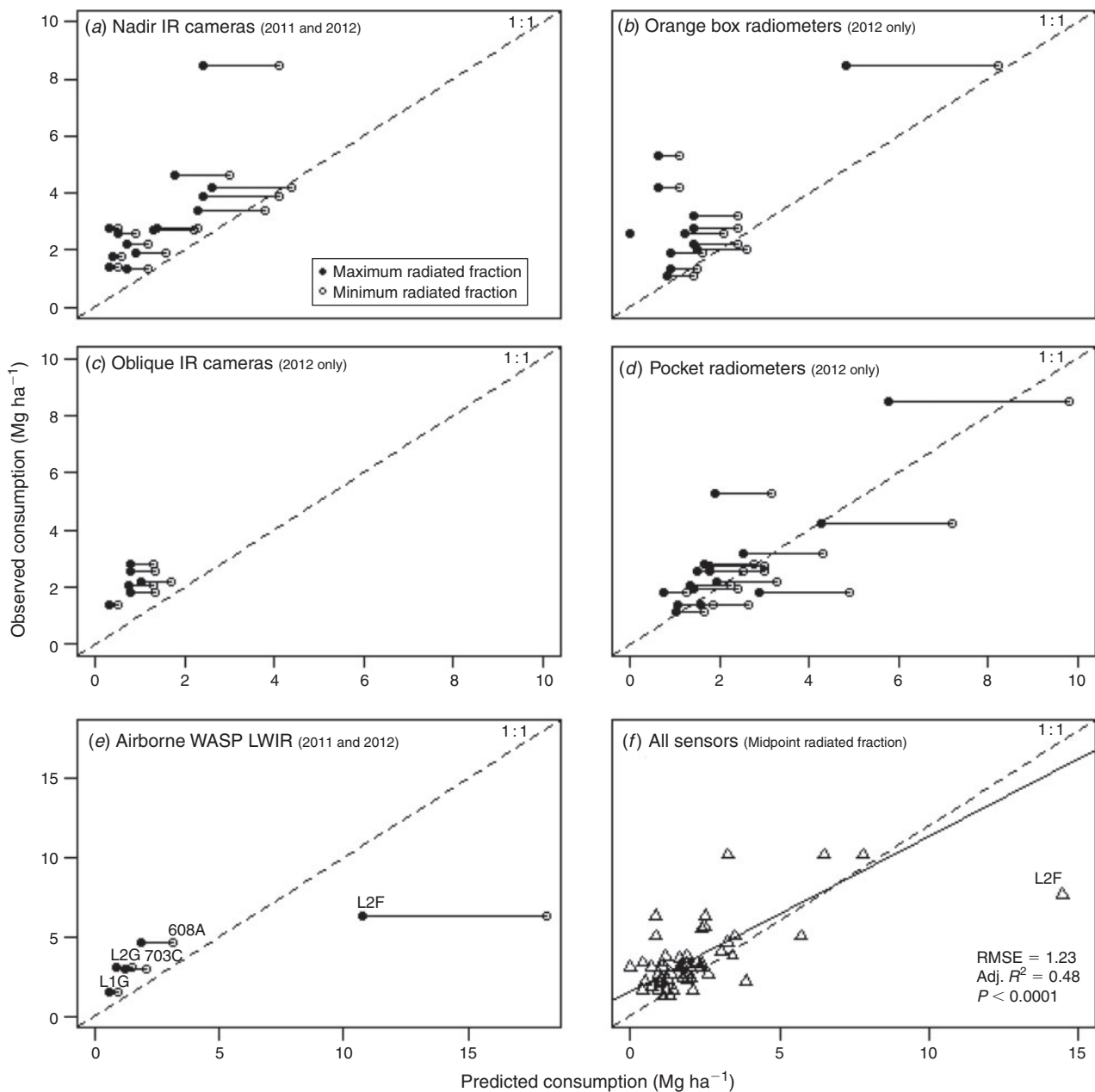


Fig. 6. Validation of fuel consumption predicted using Eqn 8 (Reid and Robertson 2012) with FRED integrated from LWIR measures collected using five different sensors: *a*) tripod-mounted, nadir-viewing IR cameras ($n = 14$); *b*) orange box radiometers ($n = 12$); *c*) boom-mounted, oblique-viewing IR cameras imaging the small (2 ha) burn blocks ($n = 6$); *d*) pocket radiometers ($n = 60$, aggregated to $n = 16$ sample units); *e*) airborne WASP LWIR imaging the large (> 100 ha) burn blocks ($n = 5$) with all bias corrections applied; and *f*) all sensors combined except the WASP LWIR outlier at large burn block L2F (labelled), with simple linear regression statistics and line of best fit. Horizontal line segments in *a–e* show expected ranges in predicted consumption based on estimated maximum or minimum radiated fraction (Kremens *et al.* 2012), indicated respectively at the lower and upper ends of each segment, whereas predicted consumption in *f*) is based on midpoint radiated fraction. Observed consumption is aggregated from clip plot biomass samples, as reported by Ottmar *et al.* (2015a).

(mean difference = 1.37 Mg ha^{-1} , s.d. = 1.43 Mg ha^{-1}), nadir IR cameras (mean difference = 1.42 Mg ha^{-1} , s.d. = 1.27 Mg ha^{-1}), and oblique IR cameras (mean difference = 1.13 Mg ha^{-1} , s.d. = 0.40 Mg ha^{-1}) (Fig. 6a–c). It is worth noting that variation among the six small (2 ha) non-forested burn blocks imaged by the oblique IR cameras (Fig. 6c) is small because by design these

were replicate burns with little variation in surface fuels among them (Ottmar *et al.* 2015a). Consumption predicted from pocket radiometers was closest of all sensors to a 1 : 1 relationship with measured consumption (Fig. 6d), with the mean difference between observed and predicted fuel consumption only 0.06 Mg ha^{-1} (s.d. = 1.06 Mg ha^{-1}). WASP-derived FRED

under-predicted consumption compared with observations, with the notable exception of the L2F burn block (Fig. 6e). Excluding L2F, the mean difference between observed and predicted consumption from among the other four large burn blocks was 1.57 Mg ha^{-1} (s.d. = 0.61 Mg ha^{-1}), or similar to the orange box radiometers and nadir and oblique IR cameras. The small mean difference between observed and predicted consumption from the pocket radiometers significantly differed from the larger mean differences calculated from the other sensor types, according to nonparametric Wilcoxon rank sum tests ($P < 0.01$ in all cases). Because the L2F burn block imaged by WASP LWIR was such an outlier, it also was excluded from a simple linear regression fit across all sensor types (Fig. 6f). We attribute the relatively high FRED values from the L2F block (Fig. 4) to greater woody and duff fuels observed in this unit, which may have been undersampled and which burn with much longer fire residence times than the fine fuels that predominated in other burn blocks. Indeed, 'virtual' firelines due to temporal undersampling are not as apparent in L2F as in the other large burn blocks (Fig. 4).

Discussion

We defined vertical height strata that are unusually narrow, within which measures of height variability (s.d., c.v.) and return density (proportion) emerged as the best predictors of surface fuel loads (Table 4). During preliminary analysis, we found the 3rd-order (skewness) and 4th-order (kurtosis) moments of the height distribution calculated within such narrowly defined height strata to not be useful, whereas the kurtosis metric calculated from the full 0–2-m height range of consideration was a significant predictor (Table 4).

To our knowledge, this paper is the first to predict surface fuel loads from airborne lidar metrics, including under forest canopies (Figs 1–3). Terrestrial lidar has been used to characterise surface fuel cells beneath longleaf pine canopies at the finer (<1 m) scales that drive fire behaviour (Hiers *et al.* 2009; Loudermilk *et al.* 2009, 2012). Attempts to predict fine fuel loads from terrestrial lidar also are thwarted by occlusion problems, but may be feasible from terrestrial lidar scanned obliquely from a boom lift (Rowell and Seielstad 2015), like the oblique-viewing IR camera imagery of the small burn blocks (O'Brien *et al.* 2015) considered in this analysis.

By design, the clip plots where fuels were measured were widely separated in space within sample units to avoid spatial autocorrelation and consequently pseudoreplication. As shown in Fig. 2, the spatial extent covered by the clip plot locations within the sample units varied greatly but was in proportion to the highly variable area of the sample units themselves. The effective sampling area within sample units varied from 0.04 ha in the 2012 HIPs ($n = 9$), to 0.16 ha in the 2011 HIPs ($n = 5$), 2 ha in the 2012 small burn blocks ($n = 6$) and ~19 ha covered by the three parallel transects within the 2012 large burn blocks ($n = 3$) (see Ottmar *et al.* 2015a for details). By pooling the surface fuel data from all the pre-fire clip plots, we treated them as independent observations in the predictive model. Spatial autocorrelation in the model errors would have constituted evidence for pseudoreplication. Although the Moran's test did find evidence of weak spatial autocorrelation in the residuals, it was not

significant ($I = 1.48$, $P = 0.07$). Therefore, adding a spatial autoregressive component to the linear model, as exemplified by Lewis *et al.* (2011) to predict surface fuel depth and percentage fuel consumption in Alaska, would have been very computationally demanding but for little profit in terms of increased predictive power or accuracy.

Local accuracy in both the maps of surface fuels predicted from lidar (Fig. 2) and maps of FRED observed by WASP LWIR (Fig. 4) was admittedly poor, as indicated by the significant but noisy relationship (not shown) between these mapped response variables at the radiometer locations (Spearman rank correlation, $\hat{\rho} = 0.50$, $P < 0.001$). This is not surprising, given the high heterogeneity in longleaf pine forest surface fuels shown by previous studies (Hiers *et al.* 2009; Loudermilk *et al.* 2009, 2012) to occur at finer scales than the 5-m resolution of our fuels map. Therefore, we chose to focus this paper on the sample unit level instead of using spatially explicit comparisons to evaluate whether we could develop reasonable corrections for overstorey canopy occlusion of the lidar and LWIR signals from the ground, and temporal and spatial undersampling by WASP LWIR.

Fire radiated fraction (Eqn 8) is a critical parameter used to estimate fuel consumption from fire radiation measurements. Despite its importance, few studies have provided estimates of fire radiated fraction or explored whether and why it might vary. The few measurements of fire radiated fraction that have been conducted in a range of wildland fuels are similar to those we used (range of 13–22%, from Kremens *et al.* 2012). For instance, Freeborn *et al.* (2011) and Wooster *et al.* (2005) report average fire radiated fractions of 11% and 14%, respectively, for a range of grass and forest fuels (recalculated on a moisture- and ash-free basis, Kremens *et al.* 2012). Wooster *et al.* (2005) found that fire radiated fraction increased with fuel consumption whereas Kremens *et al.* (2012) found no linear relationship between fire radiated fraction and fireline intensity (kW m^{-1}) or fuel consumed. Smith *et al.* (2013) reported an average fire radiated fraction of 15% that declined with fuel moisture, a variable reported by Ottmar *et al.* (2015a) but not considered in our consumption predictions, which may partially explain our tendency to underpredict consumption (Fig. 6). Clearly, the fire radiated fraction and fuel moisture variables require more attention.

The proportion of the burn block where FRFD values $> 1070 \text{ W m}^{-2}$ were never observed was also calculated as a third way to quantify fire activity that may have been missed. We did not correct for this third potential source of undersampling bias because it could overestimate FRED, as if the ground were wholly covered by a continuous surface fuelbed. A large proportion of the ground cover in the burn blocks was exposed mineral soil devoid of fuel. In fact, mineral soil was ocularly estimated in 2012 before the fires at 30 distributed post-fire clip plots per large burn block, and averaged 57.6% at L1G, 35.7% at L2G and 15.7% at L2F, in inverse proportion to pre-fire litter cover, which averaged 35.0% at L1G, 49.3% at L2G and 76.3% at L2F. These numbers reflect the time elapsed since previous burns: 1 year (L1G), 2–3 years (L2G) and 3 years (L2F). However, the continuity of the fuelbed was most conducive to fire spread in L2G among the large burn blocks, whereas the distribution of fuels in L1G would be best described as sparse,

and in L2F as very patchy. Given the complex distribution of surface fuels both between and within burn blocks, we made no attempt to account for fuel heterogeneity in this first analysis. Further, we did not attempt to account for variation in fuelbed components, but note here that consumption was dominated by the herbaceous component in the non-forest burn blocks and by the litter component in the forest blocks (Ottmar *et al.* 2015a).

Conclusions

This study is the first to predict fine surface fuel loads from airborne lidar metrics at the landscape level of prescribed fires. Riggan *et al.* (2004) estimated similar values of FRED from airborne FRFD observations at comparable spatial scales, but this study is the first to estimate FRED at the landscape scale from airborne FRFD time series collected over the full duration of the fires. The relationships between observed fuel consumption and consumption predicted from FRED approach linearity when compared across burn blocks and sensor types (Fig. 6), thus corroborating the 1 : 1 relationship between biomass combusted and FRE as found by Wooster *et al.* (2005) on small-scale experimental fires, and as expected by theory.

Future analyses will consider spatially explicit improvements for mapping these variables. For instance, one could use the known rate of fire spread (Butler *et al.* 2015), substitute space for time at the fire front observed by WASP, and use the pixels behind the fireline to represent a cooling curve, assuming uniform fuels. The surface fuels map might help to impute peak FRFD or FRED observations at the pixel level to fill in the sampling voids between apparent firelines, or geostatistical interpolation methods such as kriging could be used to fill in the gaps. Such fuel maps may also serve as useful inputs into fire behaviour models. Other datasets could also be integrated into future analyses, such as the terrestrial lidar data (Rowell and Seielstad 2015) collected across the small burn blocks and at the large burn block HIPs. We intend to make the various raw, pre-processed and final field and map data products publicly available on the USFS Research Data Archive to facilitate new fire model development and further fundamental fire science research.

Acknowledgements

This research was funded primarily by the Joint Fire Science Program (Project #11-2-1-11) with additional support from the Strategic Environmental Research and Development Program (#RC-2243). We thank Kevin Hiers and Brett Williams for essential logistical support; Clint Wright, Bob Vihnanek, Joe Restaino, Jon Dvorak, Eva Strand and Donovan Birch for fuel sampling; and Kevin Satterberg for helping to prepare data and metadata files for the RxCADRE data repository.

References

- Baskerville GL (1972) Use of logarithmic regression in the estimation of plant biomass. *Canadian Journal of Forest Research* **2**, 49–53. doi:10.1139/X72-009
- Berk A, Anderson GP, Acharya PK, Hoke M, Chetwynd J, Bernstein L, Shettle EP, Matthew MW, Alder-Golden SM (2003). MODTRAN4 version 3 revision 1 user's manual. Air Force Research Laboratory, Bedford, MA.
- Boschetti L, Roy DP (2009) Strategies for the fusion of satellite fire radiative power with burned area data for fire radiative energy derivation. *Journal of Geophysical Research* **114**, D20302. doi:10.1029/2008JD011645
- Bowman DMJS, Balch JK, Artaxo P, Bond WJ, Carlson JM, Cochrane MA, D'Antonio CM, DeFries RS, Doyle JC, Harrison SP, Johnston FH, Keeley JE, Krawchuk MA, Kull CA, Marston JB, Moritz MA, Prentice IC, Roos CI, Scott AC, Swetnam TW, van der Werf GR, Pyne SJ (2009) Fire in the earth system. *Science* **324**, 481–484. doi:10.1126/SCIENCE.1163886
- Butler B, Teskey C, Jimenez D, O'Brien J, Sopko P, Wold C, Vosburgh M, Hornsby B, Loudermilk E (2015) Observations of fire intensity and fire spread rate – RxCADRE 2012. *International Journal of Wildland Fire* **25**, 76–89. doi:10.1071/WF14154
- Dickinson MB, Hudak AT, Zajkowski T, Loudermilk EL, Schroeder W, Ellison L, Kremens RL, Holley W, Martinez O, Paxton A, Bright BC, O'Brien JJ, Hornsby B, Ichoku C, Faulring J, Gerace A, Peterson D, Mauceri J (2015) Measuring radiant emissions from entire prescribed fires with ground, airborne and satellite sensors – RxCADRE 2012. *International Journal of Wildland Fire* **25**, 48–61. doi:10.1071/WF15090
- Freeborn PH, Wooster MJ, Roberts G (2011) Addressing the spatiotemporal sampling design of MODIS to provide estimates of the fire radiative energy emitted from Africa. *Remote Sensing of Environment* **115**, 475–489. doi:10.1016/J.RSE.2010.09.017
- Hall SA, Burke IC, Box DO, Kaufmann MR, Stoker JM (2005) Estimating stand structure using discrete-return lidar: an example from low density, fire prone ponderosa pine forest. *Forest Ecology and Management* **208**, 189–209. doi:10.1016/J.FORECO.2004.12.001
- Hiers JK, O'Brien JJ, Mitchell RJ, Grego JM, Loudermilk EL (2009) The wildland fuel cell concept: an approach to characterize fine-scale variation in fuels and fire in frequently burned longleaf pine forests. *International Journal of Wildland Fire* **18**, 315–325. doi:10.1071/WF08084
- Hudak AT, Crookston NL, Evans JS, Falkowski MJ, Smith AMS, Gessler P, Morgan P (2006) Regression modeling and mapping of coniferous forest basal area and tree density from discrete-return lidar and multispectral satellite data. *Canadian Journal of Remote Sensing* **32**, 126–138. doi:10.5589/M06-007
- Kim YZ, Yang ZQ, Cohen WB, Pflugmacher D, Lauer CL, Vankat JL (2009) Distinguishing between live and dead standing tree biomass on the North Rim of Grand Canyon National Park, USA using small-footprint lidar data. *Remote Sensing of Environment* **113**, 2499–2510. doi:10.1016/J.RSE.2009.07.010
- Kremens RL, Dickinson MB, Bova AS (2012) Radiant flux density, energy density, and fuel consumption in mixed-oak forest surface fires. *International Journal of Wildland Fire* **21**, 722–730. doi:10.1071/WF10143
- Kumar SS, Roy DP, Boschetti L, Kremens R (2011) Exploiting the power law distribution properties of satellite fire radiative power retrievals – a method to estimate fire radiative energy and biomass burned from sparse satellite observations. *Journal of Geophysical Research* **116**, D19303. doi:10.1029/2011JD015676
- Lavorel S, Flannigan MD, Lambin EF, Scholes MC (2007) Vulnerability of land systems to fire: interactions among humans, climate, the atmosphere, and ecosystems. *Mitigation and Adaptation Strategies for Global Change* **12**, 33–53. doi:10.1007/S11027-006-9046-5
- Lewis SA, Hudak AT, Lentile LB, Ottmar RD, Cronan JB, Hood SM, Robichaud PR, Morgan P (2011) Using hyperspectral imagery to estimate forest floor consumption from wildfire in boreal forests of Alaska, USA. *International Journal of Wildland Fire* **20**, 255–271. doi:10.1071/WF09081
- Loudermilk EL, Hiers JK, O'Brien JJ, Mitchell RJ, Singhania A, Fernandez JC, Cropper WP, Slatton KC (2009) Ground-based LIDAR: a novel approach to quantify fine-scale fuelbed characteristics. *International Journal of Wildland Fire* **18**, 676–685. doi:10.1071/WF07138

- Loudermilk EL, O'Brien JJ, Mitchell RJ, Cropper WP, Hiers JK, Grunwald S, Grego J, Fernandez-Diaz JC (2012) Linking complex forest fuel structure and fire behaviour at fine scales. *International Journal of Wildland Fire* **21**, 882–893. doi:10.1071/WF10116
- McGaughey RJ (2014) FUSION/LDV: Software for LIDAR data analysis and visualization, Version 3.42. USDA Forest Service, Pacific Northwest Research Station (Seattle, WA)
- McKeown D, Cockburn J, Faulring J, Kremens RL, Morse D, Rhody H, Richardson M (2004) Wildfire airborne sensor program (WASP): a new wildland fire detection and mapping system. In 'Remote Sensing for Field Users: Proceedings of the Tenth Forest Service Remote Sensing Applications Conference. (CD-ROM) (Bethesda, MD: American Society of Photogrammetry and Remote Sensing).
- O'Brien JJ, Loudermilk E, Hornsby B, Hiers K, Ottmar R (2015) High-resolution infrared thermography for capturing wildland fire behavior – RxCADRE 2012. *International Journal of Wildland Fire* **25**, 62–75. doi:10.1071/WF14165
- Ottmar RD, Hudak AT, Prichard SJ, Wright CS, Restaino J, Kennedy MC, Vihnanek RE (2015a) Pre-fire and post-fire surface fuel and cover measurements collected in the southeastern United States for model evaluation and development – RxCADRE 2008, 2011 and 2012. *International Journal of Wildland Fire* **25**, 10–24. doi:10.1071/WF15092
- Ottmar RD, Hiers JK, Butler B, Clements CB, Dickinson MB, Hudak AT, O'Brien JJ, Potter BE, Rowell EM, Strand TM, Zajkowski TJ (2015b) Measurements, datasets and preliminary results from the RxCADRE project – 2008, 2011 and 2012. *International Journal of Wildland Fire* **25**, 1–9. doi:10.1071/WF14161
- R Core Team (2014) 'R: a Language and Environment for Statistical Computing.' (R Foundation for Statistical Computing: Vienna, Austria) Available at <http://www.r-project.org> [Verified 11 April 2015]
- Reid AM, Robertson KM (2012) Energy content of common fuels in upland pine savannas of the south-eastern US and their application to fire behavior modelling. *International Journal of Wildland Fire* **21**, 591–595. doi:10.1071/WF10139
- Riggan PJ, Tissell RG, Lockwood RN, Brass JA, Pereira JAR, Miranda HS, Miranda AC, Campos T, Higgins RG (2004) Remote measurement of energy and carbon flux from wildfires in Brazil. *Ecological Applications* **14**, 855–872. doi:10.1890/02-5162
- Roberts G, Wooster MJ (2008) Fire detection and fire characterization over Africa using Meteosat SEVIRI. *IEEE Transactions on Geoscience and Remote Sensing* **46**, 1200–1218. doi:10.1109/TGRS.2008.915751
- Roberts G, Wooster MJ, Freeborn P, Xu W (2011) Integration of geostationary FRP and polar orbiter burned area datasets for an enhanced biomass burning inventory. *Remote Sensing of Environment* **115**, 2047–2061. doi:10.1016/J.RSE.2011.04.006
- Robinson AP, Duursma RA, Marshall JD (2005) A regression-based equivalence test for model validation: shifting the burden of proof. *Tree Physiology* **25**, 903–913. doi:10.1093/TREEPHYS/25.7.903
- Rowell EM, Seielstad CA (2015) Development and validation of fuel height models for terrestrial lidar – RxCADRE 2012. *International Journal of Wildland Fire* **25**, 38–47. doi:10.1071/WF14170
- Schroeder W, Oliva P, Giglio L, Csiszar I (2014) The new VIIRS 375 m active fire detection data product: algorithm description and initial assessment. *Remote Sensing of Environment* **143**, 85–96. doi:10.1016/J.RSE.2013.12.008
- Seielstad CA, Queen L (2003) Using airborne laser altimetry to determine fuel models for estimating fire behavior. *Journal of Forestry* **101**, 10–15.
- Seiler W, Crutzen PJ (1980) Estimates of gross and net fluxes of carbon between the biosphere and the atmosphere from biomass burning. *Climatic Change* **2**, 207–247. doi:10.1007/BF00137988
- Smith AMS, Tinkham WT, Roy DP, Boschetti L, Kremens RL, Kumar SS, Sparks AM, Falkowski MJ (2013) Quantification of fuel moisture effects on biomass consumed derived from fire radiative energy retrievals. *Geophysical Research Letters* **40**, 6298–6302. doi:10.1002/2013GL058232
- Trigg SN, Roy DP (2007) A focus group study of factors that promote and constrain the use of satellite derived fire products by resource managers in southern Africa. *Journal of Environmental Management* **82**, 95–110. doi:10.1016/J.JENVMAN.2005.12.008
- Wooster MJ, Roberts G, Perry GLW, Kaufman YJ (2005) Retrieval of biomass combustion rates and totals from fire radiative power observations: FRP derivation and calibration relationships between biomass consumption and fire radiative energy release. *Journal of Geophysical Research, D, Atmospheres* **110**, D24311. doi:10.1029/2005JD006318
- Wooster MJ, Roberts G, Smith AMS, Johnston J, Freeborn P, Amici S, Hudak AT (2013) Thermal remote sensing of active fires and biomass burning events. In 'Thermal infrared remote sensing: sensors, methods, applications' (Eds C Kuenzer, S Dech) pp. 347–390. (Springer: Dordrecht, Germany)